Acta Pharmaceutica Sinica B 2025;15(5):2640−2654

Chinese Pharmaceutical Association
Institute of Materia Medica, Chinese Academy of Medical Sciences

Acta Pharmaceutica Sinica B

www.elsevier.com/locate/apsb
www.sciencedirect.com

ORIGINAL ARTICLE

Targeting copper homeostasis: *Akkermansia*-derived OMVs co-deliver *Atox1* siRNA and elesclomol for cancer therapy

Muhammad Hamza[a,e,†], Shuai Wang[a,b,†], Hao Wu[a,b], Jiayi Sun[a], Yang Du[a], Chuting Zeng[a], Yike Liu[a], Kun Li[a], Xili Zhu[d], Huiying Liu[c,*], Lin Chen[a,e,*], Motao Zhu[a,b,e,*]

[a]*CAS Key Laboratory for Biomedical Effects of Nanomaterials & Nanosafety, CAS Center for Excellence in Nanoscience, National Center for Nanoscience and Technology, Beijing 100190, China*
[b]*Henan Institute of Advanced Technology, Zhengzhou University, Zhengzhou 450001, China*
[c]*College of Pulmonary and Critical Care Medicine, the 8th Medical Centre, Chinese PLA General Hospital, Beijing 100039, China*
[d]*State Key Laboratory of Stem Cell and Reproductive Biology, Institute of Zoology, Chinese Academy of Science, Beijing 100101, China*
[e]*University of Chinese Academy of Sciences, Beijing 100049, China*

Received 3 December 2024; received in revised form 1 March 2025; accepted 6 March 2025

KEY WORDS

Cuproptosis;
Elesclomol;
Antioxidant protein 1 siRNA;
Outer membrane vesicle;
Akkermansia muciniphila;
Tumor microenvironment;
Cancer therapy;
Breast cancer

Abstract Cuproptosis, a recently identified form of regulated cell death triggered by excess intracellular copper, has emerged as a promising cytotoxic strategy for cancer therapy. However, the therapeutic efficacy of copper ionophores such as elesclomol (ES) is often hindered by cellular copper homeostasis mechanisms that limit copper influx and cuproptosis induction. To address this challenge, we developed a nanoagent utilizing outer membrane vesicle (OMV) derived from *Akkermansia muciniphila* (*Akk*) for co-delivery of antioxidant 1 copper chaperone (*Atox1*)-targeting siRNA and ES (siAtox1/ES@OMV) to tumors. *In vitro*, we demonstrated that *Atox1* knockdown *via* siRNA significantly disrupted copper export mechanisms, resulting in elevated intracellular copper levels. Simultaneously, ES facilitated efficient copper influx and mitochondrial transport, leading to Fe−S cluster depletion, increased proteotoxic stress, and robust cuproptosis. *In vivo*, siAtox1/ES@OMV achieved targeted tumor delivery and induced pronounced cuproptosis. Furthermore, leveraging the immunomodulatory properties of OMVs, siAtox1/ES@OMV promoted T-cell infiltration and the activation of tumor-reactive cytotoxic T cells, enhancing

*Corresponding authors.
E-mail addresses: liuhuiying@301hospital.com.cn (Huiying Liu), chenl@nanoctr.cn (Lin Chen), zhumt@nanoctr.cn (Motao Zhu).
[†]These authors made equal contributions to this work.
Peer review under the responsibility of Chinese Pharmaceutical Association and Institute of Materia Medica, Chinese Academy of Medical Sciences.

https://doi.org/10.1016/j.apsb.2025.03.014

tumor immune responses. The combination of siAtox1/ES-induced cuproptosis and immunogenic cell death synergistically suppressed tumor growth in both subcutaneous breast cancer and orthotopic rectal cancer mouse models. This study highlights the potential of integrating copper homeostasis disruption with a copper ionophore using an immunomodulatory OMV-based vector, offering a promising combinatorial strategy for cancer therapy.

1. Introduction

Copper is an essential trace element in both humans and animals and plays an indispensable role in diverse biological processes, including electron transport, mitochondrial function, iron absorption, and enzymatic activities[1-3]. Recent research has unveiled a novel form of cell death termed cuproptosis, which represents a distinct form of regulated cell death triggered by excess intracellular copper and is gaining interest as a potential therapeutic strategy in cancer therapy. Unlike other cell death mechanisms, such as apoptosis or ferroptosis, cuproptosis specifically relies on copper-induced proteotoxic stress in mitochondria, especially in tumors with high mitochondrial activity, such as breast cancer and rectal cancer[4,5].

Cuproptosis induction requires the addition of copper ionophores, such as disulfiram, 8-hydroxyquinoline, pyrithione, and elesclomol (ES)[6]. Among these, ES has been extensively evaluated in clinical trials for anti-cancer potency over the past decade, through both monotherapy and in combination with paclitaxel[7]. ES is a small molecule that binds to copper and transports it into mitochondria, leading to a continuous accumulation of copper within the mitochondria[8]. However, the clinical outcomes from multiple trials, including melanoma, ovarian epithelial cancer, prostate cancer, and other solid tumors[9-11], have shown unsatisfactory therapeutic efficacy. A key barrier to effective cuproptosis induction is the robust copper homeostatic mechanisms in cancer cells, where a network of copper chaperones and transporters work collaboratively to maintain copper levels within a physiological range[12]. This coordinated response effectively mitigates the cytotoxic effects of temporary copper influx following copper ionophore application. For example, ATOX1 (antioxidant protein 1) is a central copper chaperone for the efflux of copper from cells[13,14]. ATOX1 functions by binding intracellular copper ions and transporting copper to ATPase proteins located in the trans-Golgi network, particularly ATP7A and ATP7B, for copper export[15,16]. Previous studies have shown disruption of copper export machinery, such as genetic ablation of the *Atox1* gene, may effectively block copper efflux[17] and for efficient intracellular copper accumulation when combined with copper ionophores.

Additionally, cuproptosis-associated cellular stress may cause the release and display of tumor-associated antigens to increase tumor immunogenicity. Under this scenario, a significant number of tumor-infiltrated T cells may execute effective tumor killing, leading to immunogenic cell death (ICD)[18]. Given this background, it is advantageous to develop combinatorial therapeutic strategies that can simultaneously induce cuproptosis and inflame the tumor immune microenvironment (TIME) to effectively eliminate tumors.

Triple-negative breast cancer (TNBC) and colorectal cancer (CRC) represent two of the most lethal forms of cancers[19], characterized by elevated copper concentration in patient serum and tumors[20,21], which heightens their susceptibility to cytotoxicity generated by cuproptosis. However, the immune environment of TNBC[22] and CRC[23] are well-documented as immunosuppressive. Therefore, we selected an immunomodulatory outer membrane vesicle (OMV) as an immune-active vector for the co-delivery of cuprotosis-inducing copper ionophore ES. OMV is nanoscale, spherical vesicle (20−250 nm) released from Gram-negative bacteria, harboring a diverse range of bioactive substances such as antigens, pathogen-associated molecular patterns (PAMPs), toxins, and virulence factors in a strain-specific pattern[24]. These vesicles have been explored for various biomedical applications, including cancer immunotherapy, drug delivery, and adjuvants[25]. Among the abundant bacteria origins, OMV derived from the *Akkermansia muciniphila* (*Akk*), a probiotic bacterium that represents 3%−5% of the microbial composition in the healthy human gut[26,27], has shown immune-modulatory effect in toll-like receptor signaling and ability in improving immune checkpoint therapy[28,29], making it an excellent candidate for TIME reprograming as well as drug delivery[30].

In this study, we employed *Akk*-derived OMV for the co-delivery of *Atox1* siRNA and ES to induce cuproptosis and stimulate anti-tumor immune responses. We show that systemic administration of siAtox1/ES@OMV significantly inhibited tumor growth in both subcutaneous breast cancer and orthotopic rectal cancer mouse models. This innovative approach not only addresses the limitations of traditional copper ionophore-based therapies but also harnesses the potential of immunomodulation of OMV, offering a promising combinatorial approach in treating high-copper and immune-cold tumors.

2. Materials and methods

2.1. Materials

Elesclomol (AY0434) was purchased from AIYAN (Shanghai, China). $CuCl_2 \cdot 2H_2O$ (CAS 10125-13-0) was purchased from Sangon Biotech (Shanghai, China). Dulbecco's modified eagle medium (319-005-CL), RPMI 1640 medium, and fetal bovine serum (085−150) were obtained from Wisent Bio Products (St. Bruno, Canada). Brain Heart Infusion medium (LA0360) was purchased from Solarbio Life Science (Beijing, China). XenoLight D-Luciferin K^+ Salt Bioluminescent Substrate (122799) was obtained from PerkinElmer (PE, USA). Radio immunoprecipitation assay (RIPA) lysis buffer (R0010), PMSF (P0100), and Red Blood Cell Lysis Buffer (R1010) were purchased from Solarbio Life Science (Beijing, China). GAPDH (rabbit monoclonal antibody; 5174) and anti-rabbit IgG (7074S) were purchased from Cell Signaling Technology (CST, USA). LIAS (rabbit monoclonal antibody, 11577-1-AP) was purchased

from Proteintech (Wuhan, China). FDX (rabbit monoclonal antibody, EPR4629) was purchased from Abcam (Cambridge, UK). Mouse IL-6 (M6000B) was purchased from Bio-Techne (Minnesota, USA). ELISA MAX^{TM}IFN-α Deluxe Set Mouse IFN-α1 (447904) was purchased from BioLegend (San Diego, USA). DNase I (D7073) was purchased from Beyotime (Shanghai, China). Collagenase type IV (C8160) and hyaluronidase (H8030) were purchased from Solarbio. VioletFluor™ 450 anti-mouse CD45 (83090S) and anti-mouse MHC Class II-violetFluor™ 450 (86628) were purchased from CST (MA, USA). Super Bright ™ 702 anti-mouse CD3 (67-0032-82) and Super Bright ™ 600 anti-mouse CD4 (63-0041-80) were purchased from eBioscience (San Diego, CA, USA). Anti-mouse CD16/CD32 (101302), PE/Cy7 anti-mouse CD8 (100722), and anti-mouse CD11c-Brilliant Violet 605™ (117334), anti-mouse CD11b-Alexa Fluor® 700 (101222), anti-mouse CD80-PE-Cy7 (104733), anti-mouse CD86-APC (105113), and anti-mouse MHC Class I-PE (114608) and APC anti-mouse IFN-γ (505810) were purchased from BioLegend (San Diego, USA).

2.2. Methods

2.2.1. Cell culture

4T1 murine mammary carcinoma cells, MDA-MB-231 human breast cancer cells, and CT26-Luc murine mammary carcinoma cells were obtained from the American Type Culture Collection (ATCC, Manassas, USA). 4T1 and MDA-MB-231 were cultured in DMEM medium containing 10% fetal bovine serum and 1% penicillin−streptomycin (WISENT, St. Bruno, Canada). CT26-Luc was cultured in RPMI 1640 medium containing 10% fetal bovine serum and 1% penicillin−streptomycin. All cells were incubated at 37 °C in 5% CO_2 and confirmed to be mycoplasma-free.

2.2.2. Bacteria culture and isolation of OMV

Akk (BAA-835) was purchased from the ATCC and cultured in Brain Heart Infusion (BHI) broth at 37 °C under an anaerobic atmosphere consisting of 90% N_2, 5% H_2, and 5% CO_2. Once the culture reached an optical density of 0.5−0.6 at 600 nm (OD_{600}), the bacterial cells were removed through centrifugation (Eppendorf, 5810R, Hamburg, Germany) at 8000×*g* for 20 min at 4 °C. The resulting supernatant was filtered using a 0.45-μm EPS filter (R8SA47939, Millipore), and concentrated to 30 mL using a 100-K ultrafiltration tube (UFC710008, Millipore). The concentrated solution was further processed using a 0.22-μm EPS membrane (R3EA06699, Millipore). OMV was collected from the filtrate by ultracentrifugation (Beckman, OPTIMA XPN-100, CA, USA) at 150,000×*g* for 1.5 h at 4 °C and then resuspended in 400 μL of PBS. The resuspended OMV was passed through a 0.22-μm filter and stored at −80 °C until use. The total protein concentration of OMV was assessed using the bicinchoninic acid assay.

2.2.3. Preparation of siAtox1@OMV, ES@OMV, and siAtox1/ES@OMV

To prepare siAtox1@OMV, 12 μg of siAtox1 was loaded into 200 μg of OMV using electroporation (400 V, 125 μF) with the Gene Pulser Xcell™ Electroporation System (Bio-Rad, CA, USA). For ES@OMV preparation, 1 mg of ES (dissolved in 20 μL of DMSO) was loaded into 200 μg OMV using the same electroporation conditions. ES was dissolved according to MCE's formulation protocol. The solubilization process involved the sequential addition of 10% DMSO as the primary solvent, followed by 40% PEG300, with subsequent homogenization. The formulation was further optimized by incorporating 5% Tween-80 as a surfactant, and the final volume was adjusted with 45% normal saline. This optimized formulation system exhibited enhanced solubilization capacity, achieving ES solubility over 2.5 mg/mL. For siAtox1/ES@OMV, both 12 μg of siAtox1 and 1 mg of ES were simultaneously loaded into 200 μg OMV using the same electroporation parameters. After electroporation, the samples were transferred to 50-K ultrafiltration tubes and centrifuged at 5000 rpm for 5 min. The samples retained in the ultrafiltration tubes were then washed three times with PBS.

2.2.4. Characterization of OMV

The morphology, particle size, zeta potential, and polydispersity index (PDI) of the OMV were characterized by using TEM HT7700 (UK) and a Zetasizer Nano ZS dynamic light scattering instrument (Malvern Instruments, UK), respectively. For TEM imaging, OMV was deposited on 200 mesh copper grids for 20 min, followed by negative staining with 2% uranyl acetate for 3 min. The prepared grids were then examined using TEM at 120 kV. For the measurement of size, zeta potential, and PDI of OMV, samples were prepared by suspending the vesicles in deionized water (ddH_2O) at a concentration of 50 μg/mL total protein. These samples were then analyzed using the Zetasizer Nano ZS dynamic light scattering instrument.

2.2.5. Drug release analysis

siAtox1/ES@OMV (1 mL) was loaded in 2 kDa dialysis devices and immersed in 50 mL of PBS (pH 7.4) containing 0.1% Tween 80, followed by shaking at 100 rpm at 37 °C. To monitor the drug release kinetics, a sample of 50 μL was collected from the outer medium at different time intervals (0, 20, 35, 60, 120, 240, 360, 480, and 720 min). The concentration of ES in each sample was analyzed and quantified using HPLC (LC-20AT, Shimadzu, Kyoto, Japan) with a Poroshell 120 EC-C18 column (2.7 μm, 150 mm × 3.0 mm, Agilent Technologies, Santa Clara, CA, USA). The mobile phase consisted of a mixture of water with 0.1% trifluoroacetic acid (TFA) and acetonitrile with 0.1% TFA, in a ratio of 57:43. The chromatographic separation was performed at a flow rate of 0.3 mL/min, with the eluent monitored at 274 nm for ES detection.

2.2.6. Confocal microscopy of siAtox1/ES@OMV

To assess the cellular uptake and intracellular localization of siAtox1/ES@OMV, 4T1 cells were incubated with freshly prepared Cy5-labeled siAtox1/ES@OMV for 1, 3, and 6 h. Lysosomes were stained with Lyso-Tracker (L7526, Thermo, USA), and nuclei were stained with Hoechst 33342 (C0030, Solarbio, China). The cells were observed under a confocal microscope (Zeiss LSM710, Germany).

2.2.7. OMV-induced BMDC immunogenicity analysis

To investigate whether the OMVs have the potential to enhance the immunogenicity of BMDCs, the cells were seeded in 12-well plates and incubated with OMV at a protein concentration of 20 μg/mL. After 12 h of treatment, supernatants were collected for cytokines analysis. Following 24 h of treatment, BMDCs were stained with anti-mouse CD11c-BV605, anti-mouse CD80-PE/Cy7, anti-mouse CD86-APC antibodies, anti-mouse MHC-I-PE, and anti-mouse MHC−II−violetFluor™ 450 antibodies to assess their maturation *via* flow cytometry.

2.2.8. In vivo biodistribution of siAtox1/ES@OMV

To assess the biodistribution of siAtox1/ES@OMV *in vivo*, Cy5-labeled siAtox1/ES@OMV (60 μg protein per mouse) was administered to 4T1 tumor-bearing mice *via* tail vein injection. At 24 h post-injection, the mice were imaged using an IVIS spectrum system (PerkinElmer, USA), and the major organs and tumors were harvested for *ex vivo* imaging. The fluorescent signal was quantified using biphotonic imaging.

2.2.9. Mouse experiments

Female BALB/c mice (6−8 weeks old) were purchased from SPF Biotechnology Co., Ltd. (Beijing, China). The animals were maintained in a controlled environment with a temperature of 20−25 °C and relative humidity between 30% and 70%. All animal protocols were approved by the Institutional Animal Care and Use Committee of the National Center for Nanoscience and Technology.

To establish 4T1 subcutaneous tumor models, BALB/c mice were subcutaneously inoculated with 2×10^6 4T1 cells on the right flank. Four days post-inoculation, the mice were randomly assigned to experimental groups (5 mice/group): 1) PBS control; 2) siAtox1@OMV; 3) ES@OMV; and 4) siAtox1/ES@OMV (60 μg OMV per mouse), by tail vein injections in a volume of 100 μL on Days 4, 7, 10, 14, and 18 post tumor inoculation. The volumes of all tumors were measured with electronic calipers every other day and calculated according to Eq. (1):

$$V = (\text{Length} \times \text{Width}^2)/2 \quad (1)$$

Additionally, the weights of the mice were recorded every 2 days. The mice were euthanized on Day 20. Serum was collected for the measurement of cytokine levels. Tumors were excised, weighed, and digested into single-cell suspensions for analysis of infiltrating immune cells *via* flow cytometry.

To establish the CT26-Luc orthotopic mouse model, female BALB/c mice were subcutaneously inoculated with CT26-Luc colon tumor cells. Once the tumor volume reached 200−300 mm^3, the tumors were excised, dissected into fragments of approximately 8−10 mm^3, and grafted onto the cecum of BALB/c mice. Seven days after grafting, mice were assigned to two groups: the PBS control group and the siAtox1/ES@OMV treatment group (60 μg OMV per mouse), 3 mice were tested in each group. Treatments were administered on Days 7, 10, 13, 16, and 18. An IVIS (PerkinElmer) was used to monitor the bioluminescence signal generated by the orthotopic tumor. In the PBS group, one mouse with a large tumor in the intestine could not be detected by the bioluminescence imaging (BLI). D-luciferin (150 mg/kg; PerkinElmer, USA) was administered by intraperitoneal injection 10 min before imaging. On Day 20, the mice were euthanized. Subsequently, tumors were carefully excised, weighed, and digested into a single-cell suspension for Cytometry by Time-of-Flight (CyTOF) analysis.

To evaluate and quantify the synergistic effects of the siAtox1/ES@OMV in cancer therapies, we applied the Bliss definition and the Bliss independence model for assessment. Tumor weight data were analyzed using the following three groups of animals: siAtox1@OMV (A), ES@OMV (B), siAtox1/ES@OMV (C). Before performing calculations, the tumor weight (TW) data are first normalized ($0 \leq \text{Effect} \leq 1$) as shown in Eq. (2):

$$\text{Effect (E)} = 1 - \frac{TW - TW(min)}{TW(max) - TW(min)} \quad (2)$$

Following Bliss's definition, the synergistic effect is calculated using the Bliss independence model, according to Eq. (3):

$$\text{Synergy index} = \frac{E(C)}{[E(A) + E(B) - E(A) \times E(B)]} \quad (3)$$

When the synergy index is < 1, it indicates a synergistic effect. When it equals 1, it indicates an additive effect. When it is > 1, it indicates an antagonistic effect.

2.2.10. Flow cytometry and CyTOF analysis

Tumor tissues were minced and incubated in 2 mL of digesting solution (RPMI 1640 containing 1.5% FBS, 1 mg/mL collagenase type IV, 0.02 mg/mL DNase I, and 0.1 mg/mL hyaluronidase). These samples were incubated for 60 min at 37 °C with shaking at 200 rpm, followed by incubation in RBC lysis buffer (Solarbio) and filtration through a 40 μm cell strainer to obtain single-cell suspensions. The isolated cells were cultured in complete RPMI 1640 medium in the presence of BD Golgi STOP^T for 4−6 h at 37 °C. To minimize nonspecific Fc receptor binding, the tumor cells were pre-incubated with anti-mouse CD16/CD32 (Biolegend) for 30 min at 4 °C. For analysis of tumor-infiltrated T cell populations, cells were stained with VioletFluor™ 450 anti-mouse CD45, Super Bright™ 702 anti-mouse CD3, Super Bright™ 600 anti-mouse CD4, and PE/Cy7 anti-mouse CD8 at 4 °C for 30 min. After surface staining, a fixation/permeabilization buffer set (eBioscience, San Diego, CA, USA) solution was added. Post fixation and permeabilization, the cells were stained with APC anti-mouse interferon (IFN)-γ. Fluorescent signals were assessed using an Attune NxT flow cytometer (Thermo, USA), and the data were analyzed with FlowJo software (FlowJo LLC, US).

For CyTOF analysis, single-cell suspensions were prepared as a similar procedure for flow cytometry. The single-cell suspensions were first stained with 0.01% cisplatin for 2 min, followed by fixation with 1.6% paraformaldehyde for 15 min. Subsequently, the cells were stained with metal-labeled antibodies against CD45, CD3, CD4, CD8, CD11b, and F4/80. The cells were then stained with 0.1% Ir (Fluidigm, South San Francisco, CA, USA) at 4 °C overnight. The following day, the cells were washed and prepared for acquisition with the Helios system (Fluidigm, South San Francisco, CA, USA). Data analysis and generation of *t*-distributed stochastic neighbor embedding (*t*-SNE) maps were performed using Cytobank (cytobank.org).

2.2.11. Atox1 siRNA

The small interfering RNA targeting mouse *Atox1* (siAtox1) and Cy5-labeled siRNA sequence used in this study was: 5′-GAGGAGTGGAGTTCAACAT-3′.

2.2.12. RNA extraction and reverse transcription-quantitative PCR (RT-qPCR)

Total RNA was extracted from 4T1 cells and mouse tumor tissues using TRIzol reagent (Invitrogen). First-strand cDNA was synthesized by reverse transcribing 2 μg of total RNA with the HiFiScript cDNA Synthesis Kit (Jiangsu CoWin Biotech Co.). The expression levels of *Atox1* were measured using RT-qPCR on a Bio-Rad CFX96 system. Relative quantification was calculated by the $2^{-\Delta\Delta Ct}$ calculation normalized against β-actin. Primer sequences (5′−3′) were as follows: *Atox1*-F: ATGCCGAAGCACGAG TTCTC; *Atox1*-R: ATGCAGACCTTCTTGTTGGGC. β-actin-F: GGCTGTATTCCCCTCCATCG; β-actin-R: CCAGTTGGTAA CAATGCCATGT.

2.2.13. Western blotting

Homogenized tumor tissues and collected cultured cells were lysed in RIPA lysis buffer containing 1 mmol/L protease inhibitor and phosphatase inhibitor. The lysates were incubated on ice for 30 min, followed by centrifugation at 13,000×*g* for 20 min at 4 °C. The supernatant was collected and quantified using the BCA protein assay (Solarbio). The protein solution was then mixed with 4 × loading buffer (Invitrogen) and heated at 100 °C for 10 min. Equal proteins (20 μg) were loaded onto 12% SDS-PAGE and subjected to electrophoresis initially at 80 V for 30 min, followed by 120 V for 60 min. Separated proteins were transferred onto 0.22 μm PVDF membranes at 300 mA for 90 min. After blocking with 1 × TBST containing 5% powdered milk for 120 min, the membranes were probed with primary antibodies followed by secondary antibodies at room temperature for 2−4 h. Chemiluminescence detection was performed using the Invitrogen Novex ECL Chemiluminescent Substrate Reagent Kit on a Bio-Rad ChemiDoc™ imaging system.

2.2.14. Generation of Atox1 knockout cells

The sgRNA sequence used for targeting *Atox1*: 5′-TGCA-GACCTTCTTGTTGGGC-3′. The annealed sgRNA oligos were cloned into the lentiCRISPR V2 vector (Addgene). For lentiviral packaging, the resulting plasmids were co-transfected with the psPAX2 and pMD2.G into HEK293T cells. The lentiviral particle-containing medium, collected from the supernatant of transfected HEK293T cells, was used to infect 4T1 cells. Following infection, cells were selected using 1 μg/mL puromycin. After a 10-day incubation period, individual clones were isolated, expanded, cryopreserved, and cultured into 6-well plates. The successful *Atox1* knockout clones were verified using RT-qPCR.

2.2.15. Cell migration assay

To assess cell migration, 8 μm pore-sized plain transwell inserts (Costar, High Wycombe, UK) were plated in the wells of 24-well culture plates. 4T1 wildtype and *Atox1* KO cells were seeded at a density of 5×10^4 cells per well in the top chambers containing serum-free DMEM. The lower chambers were filled with 600 μL of DMEM medium containing 10% FBS. After a 16 h incubation at 37 °C, cells that had migrated to the lower surface of the membrane were fixed and stained with 0.05% crystal violet in 20% ethanol for 5 min. The inserts were washed several times with PBS to remove excess dye. Cells remaining in the upper compartment were gently removed with a cotton swab. The inserts were allowed to dry completely, and images were taken. For the experiments involving OMV, cells were treated in the upper chamber with 10 μL of siAtox1@OMV, ES@OMV, or siAtox1/ES@OMV combined with 10 μmol/L $CuCl_2$. After 18 h of incubation, cells were also fixed and stained with crystal violet and observed for migration.

2.2.16. Cell viability

Cell viability was assessed using the CCK8 assay. 4T1 cells were seeded into 96-well plates at a density of 5000 cells per well. After 24 h, the cells were treated with the indicated formulations in the presence of 10 μmol/L $CuCl_2$ in culture medium for another 24 h. Subsequently, 10 μL of CCK8 solution was added to each well, and the plates were incubated at 37 °C for 2 h. Absorbance was measured at a wavelength of 490 nm using a microplate spectrophotometer.

2.2.17. Enzyme-linked immunosorbent assays (ELISA)

The levels of IL-6 and IFN-α were measured using ELISA. Briefly, at the endpoint of the mouse experiment, 3 h after the final intravenous injection, blood samples were collected and incubated at RT for 1 h. The samples were centrifuged at 3000 rpm for 15 min at 4 °C to collect the serum. The serum was diluted 5-fold to measure the content of cytokines using the ELISA kit (BioLegend, San Diego, USA).

2.2.18. Inductively coupled plasma-mass spectrometry (ICP−MS)

Copper content was analyzed by ICP−MS (PerkinElmer, NexION 300D, Norwalk, USA). Samples containing 100 μg of protein from either 4T1 wildtype or *Atox1* KO cells were digested in 200 μL of HNO_3 at 100 °C for 4 h. The resulting clear solution was then diluted to a final volume of 5 mL with 2% nitric acid. The samples were then analyzed by an ICP−MS operating in kinetic energy discrimination mode, and copper concentrations were determined by comparison against a calibration curve of known copper standards.

2.2.19. Statistical analysis

Data are presented as the mean ± standard deviation (SD). At least three independent experiments were performed for each *in vitro* study. Statistical analysis was performed using a two-tailed unpaired *t*-test or a one-way ANOVA with Tukey's multiple comparisons test for the comparison of two groups, and a two-way ANOVA followed by Bonferroni post-test analysis for the comparison of more than two groups of data. Data analysis was facilitated by GraphPad Prism 5 (GraphPad Software, US), FlowJo V10 (FlowJo LLC, US), and ImageJ v1.8.0 (The National Institutes of Health, US) software. Statistical significance was set as follows: $^*P < 0.05$; $^{**}P < 0.01$; $^{***}P < 0.001$; NS, not significant.

3. Results

3.1. Atox1 depletion enhances ES cytotoxicity in breast cancer cells

To test the potential of silencing the *Atox1* gene in improving ES-induced cuproptosis in breast cancer cells, we first employed a CRISPR-Cas9-mediated system to generate *Atox1* knockout (KO) 4T1 cell lines. Using QPCR analysis, we showed that the transcriptional level of the *Atox1* gene was significantly down-regulated in the *Atox1* sgRNA-transduced cells (Supporting Information Fig. S1A). Cell growth was inhibited in the *Atox1*-KO cells (Fig. S1B). We further applied ICP−MS for the measurement of intracellular copper content and showed a significantly higher copper content in the *Atox1*-KO cells compared to the wild-type (WT) cells (Fig. S1C), suggesting that the absence of *Atox1* indeed hampered copper export in cancer cells. As a consequence, the cytotoxicity induced by the copper ionophore ES was markedly enhanced in *Atox1*-KO cells (IC_{50} 97.42 nmol/L) compared to WT cells (IC_{50} 124.9 nmol/L). Such effect was further exacerbated by a conditioned cell culture medium supplemented with 10 μmol/L $CuCl_2$, where the IC_{50} of ES for *Atox1*-KO cells (22.17 nmol/L) was approximately 3-fold lower than that for *Atox1* WT cells (68.34 nmol/L) (Fig. S1D). Collectively, the results suggest that the depleting *Atox1*-mediated copper

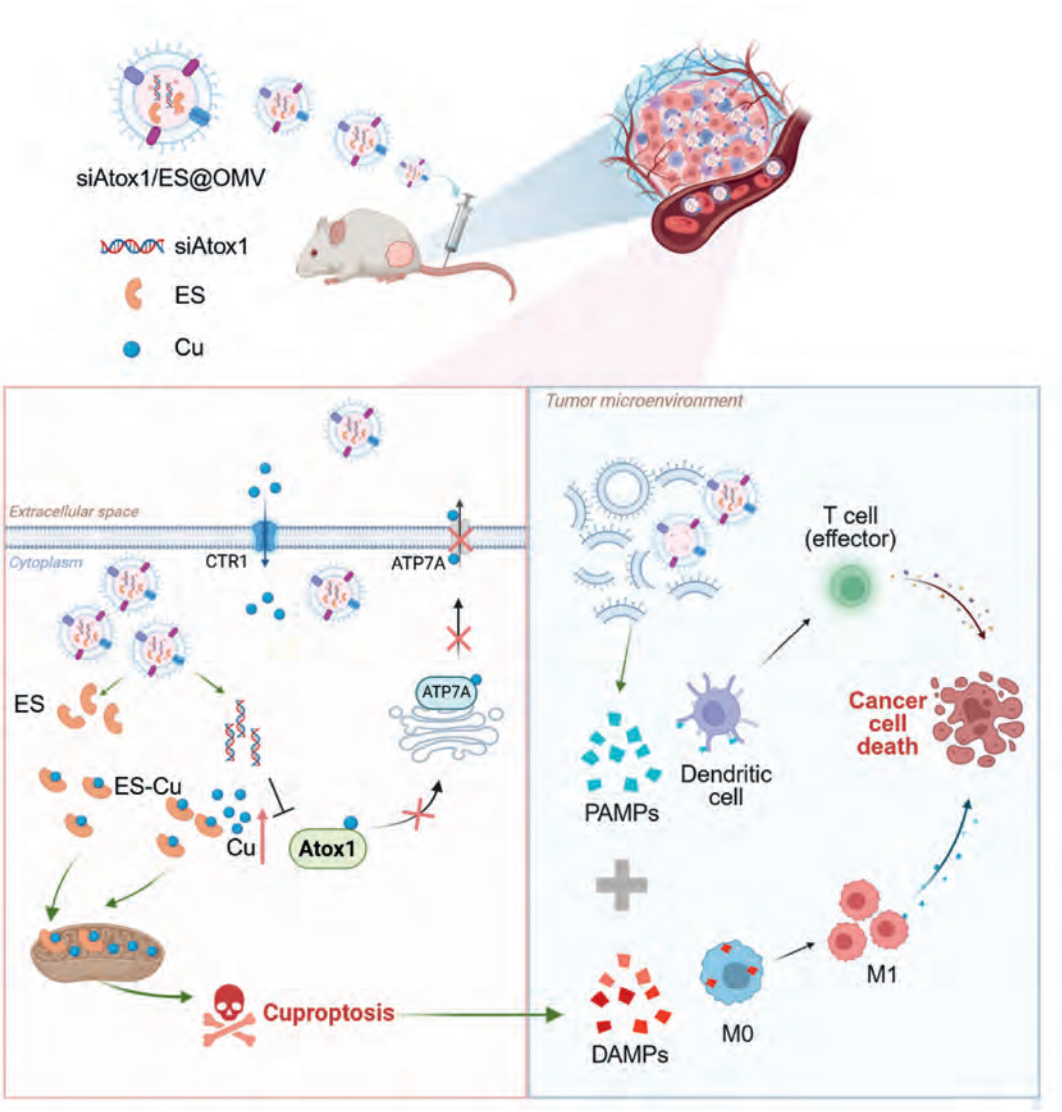

Figure 1 Schematic illustration of the fabrication process of siAtox1/ES@OMV and the working mechanism for anti-tumor therapy.

exportation combined with ES-mediated copper importation generates strong cytotoxicity for breast cancer cells.

We next develop a nanomedicine for the co-delivery of ES and *Atox1*-targeting siRNA using *Akk*-derived OMV[31] for a combinational effect for cuproptosis induction and immunoactivation in anti-tumor therapy. Fig. 1 illustrates the proposed working mechanism of siAtox1/ES@OMV in tumor therapy. Upon systemic administration, we proposed that the siAtox1/ES@OMV, with a nanosize-facilitated enhanced pemealization effect (EPR), could efficiently traffick to tumor regions, where they trigger cuproptosis in cancer cells through the dual-function mechanism. Secondly, the release of damage-associated molecular patterns (DAMPs) by cuproptosis, in conjunction with PAMPs from the OMV, may effectively reprogram the tumor immune microenvironments for anti-tumor immune responses.

3.2. *Preparation and characterization of siAtox1/ES@OMV*

Akk-OMV was isolated from the culture medium of *Akk* until OD_{600} nm reached 0.5−0.6. After removing the bacteria through centrifugation, the supernatant was subjected to filtration *via* a 0.45-μm filter and concentrated using a 100-K ultrafiltration tube. The concentrated solution underwent further filtration using a 0.22-μm membrane. OMV was purified from the filtrate by ultracentrifugation at 150,000×*g* for 1.5 h and subsequently resuspended in PBS. Following purification, the physicochemical properties and molecular composition of OMV were comprehensively characterized. Scanning transmission electron microscopy with energy-dispersive X-ray spectroscopy (STEM-EDX) was performed to analyze the detailed elemental composition of the OMV. The STEM-EDX mapping revealed the spatial distribution and relative abundance of key elements in OMV, including carbon (C), nitrogen (N), oxygen (O), phosphorus (P), and sulfur (S) (Supporting Information Fig. S2A). The protein composition of *Akk*-OMV was initially analyzed by Coomassie blue staining (Fig. S2B) and further characterized using liquid chromatography-tandem mass spectrometry (LC−MS/MS). To ensure reproducibility and identify core components, two OMV samples were analyzed independently. Proteomic analysis identified 48 and 43 proteins in sample 1 and sample 2, respectively, with 21 proteins consistently detected in both samples (Fig. S2C). Notably, a significant portion of the identified proteins were membrane proteins,

12 of which are shared between both samples (Fig. S2D). This substantial overlap in protein composition, particularly membrane proteins, suggests the existence of a conserved core proteome that likely plays essential structural and functional roles in OMV biology. In addition, the average hydrodynamic diameter of OMV remained unchanged at 4 and 37 °C for 7 days (Fig. S2E), further supporting their high stability, robustness, and suitability for downstream applications.

siAtox1 and ES were loaded either separately or in combination into OMV through electroporation, resulting in siAtox1@-OMV, ES@OMV, and siAtox1/ES@OMV, respectively (Fig. 2A). The TEM micrograph revealed *Akk*-OMV exhibited a spherical lipid bilayer morphology (Fig. 2B). The loading of siAtox1 or ES did not alter the morphology of *Akk*-OMV, although a slight increase in particle size was observed. The average hydrodynamic diameter of 100.18 ± 23 nm (*Akk*-OMV), 185.1 ± 18 nm (siAtox1@OMV), 164.4 ± 16 nm (ES@OMV), and 212.35 ± 23 nm (siAtox1/ES@OMV) were determined by dynamic light scattering (DLS) measurement (Fig. 2C). The surface charges of *Akk*-OMV, siAtox1@OMV, ES@OMV, and siAtox1/ES@OMV were −18.2, −30.1, −18.5, and −20.2 mV, respectively (Fig. 2D), with the polydispersity index (PDI) all below 0.4 in an aqueous solution (Fig. 2E). We next calculated the encapsulation efficiency using Cy5-labeled siAtox1 and showed an encapsulation efficiency of approximately 70% for siAtox1 based on fluorescence intensity (Supporting Information Fig. S3A). The siAtox1 loading efficiency was also measured by nucleic acid gel electrophoresis, which compared the unencapsulated siAtox1 in the OMV mixture before and after electroporation. The results showed that electroporation facilitated the encapsulation of approximately 70% of siAtox1 into OMV (Fig. S3B). The encapsulation efficacy of ES was 12.3% as determined by HPLC at A274 nm (Fig. S3C−S3E). The accumulative ES release was approximately 40% in 12 h in PBS buffer (pH 7.4) containing 0.1% Tween 80 (Fig. 2F).

3.3. *In vitro cellular uptake and cytotoxicity of siAtox1/ES@OMV*

To investigate the intracellular uptake of siAtox1/ES@OMV and the lysosomal escape of siAtox1, siAtox1 was labeled with a Cy5 dye prior to loading into OMV. The fluorescence intensity of Cy5 (red) in 4T1 cells at 1, 3, and 6 h post-incubation was visualized

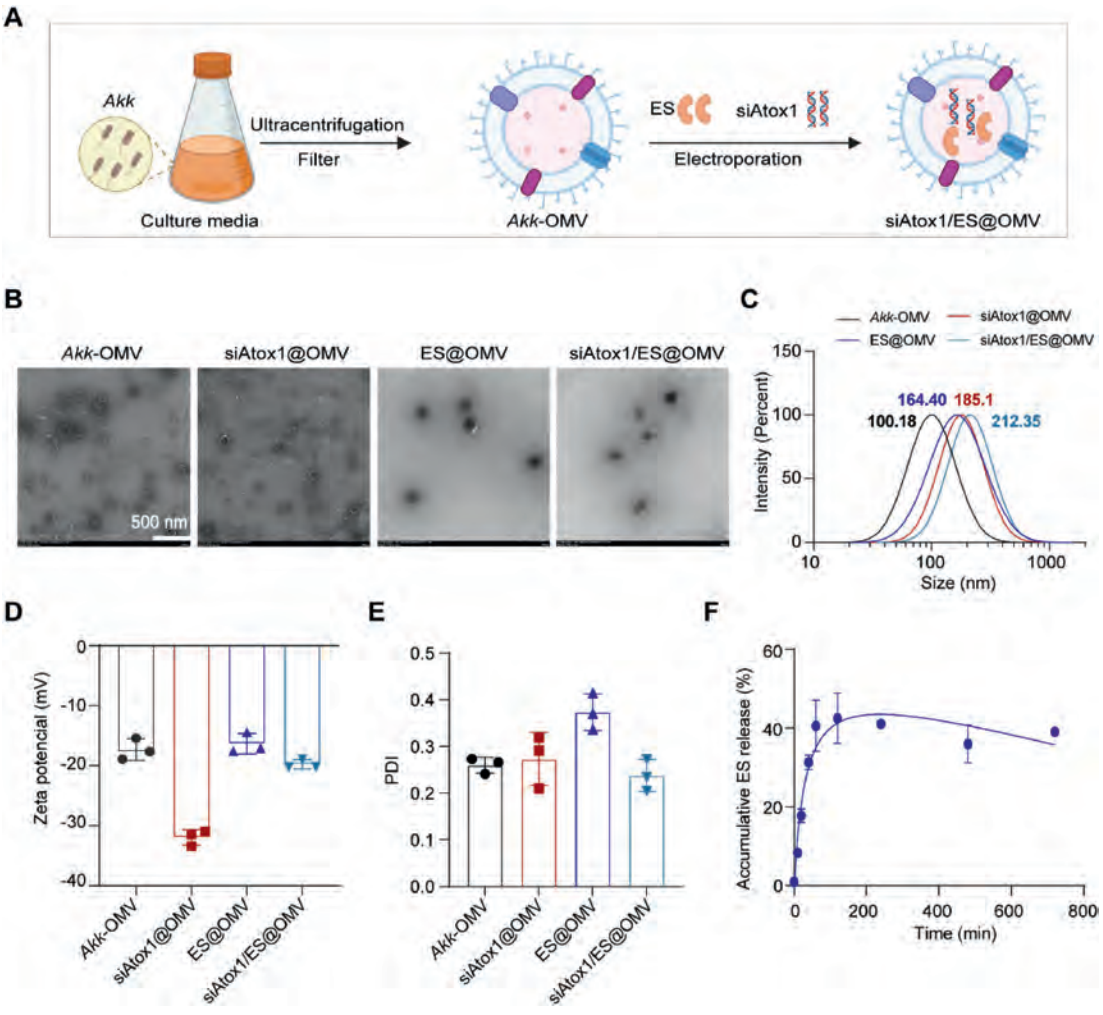

Figure 2 Characteristics of siAtox1/ES@OMV. (A) Schematic illustration of the fabrication process of siAtox1/ES@OMV. (B) TEM images of *Akk*-OMV, siAtox1@OMV, ES@OMV, and siAtox1/ES@OMV. Scale bars: 500 nm. (C−E) The average size (C), zeta potentials (D), and polydisperse index (E) of *Akk*-OMV, siAtox1@OMV, ES@OMV, and siAtox1/ES@OMV determined by DLS. (F) *In vitro* release kinetics of ES from siAtox1/ES@OMV at pH 7.4 (PBS containing 0.1% Tween-80).

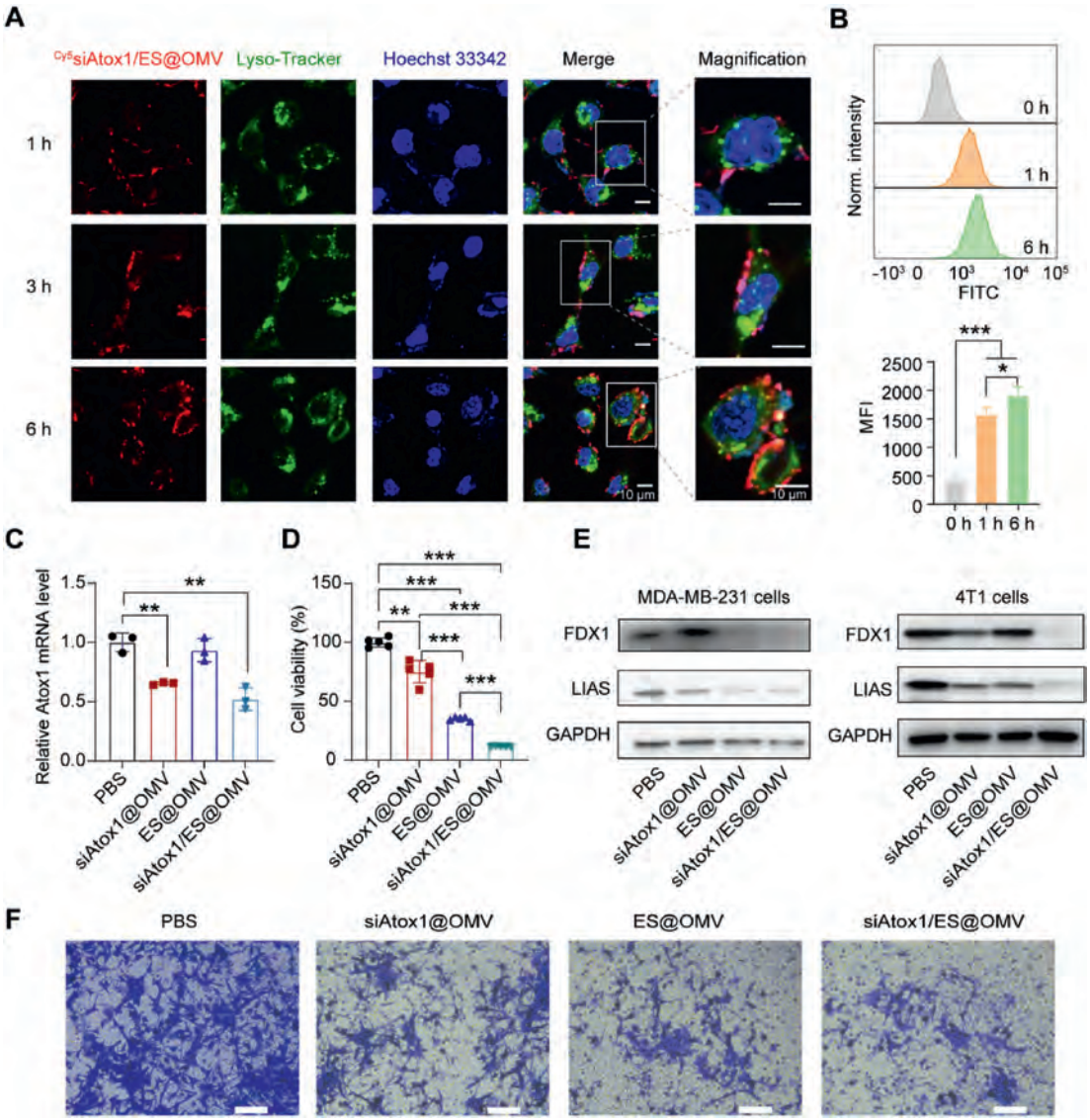

Figure 3 The intracellular uptake of siAtox1/ES@OMV and induction of cuproptosis *in vitro*. (A) Confocal images of 4T1 cells incubated with cy5-siAtox1@OMV for 1, 3, and 6 h, respectively. The lysosome was stained with Lyso-Tracker (Green), nucleus was stained with Hoechst 33342 (Blue). (B) Flow cytometry analysis of 4T1 cells after incubation FITC-labeled siAtox1/ES@OMV for 0, 1, and 6 h. Median fluorescence intensity (MFI) was quantified and shown in the right panel. (C) RT-qPCR analysis of the relative *Atox1* mRNA expression in 4T1 cells treated with siAtox1@OMV, ES@OMV, and siAtox1/ES@OMV for 24 h. Data are represented as the mean ± SD ($n = 3$). (D) CCK8 analysis of 4T1 cells treated with siAtox1@OMV, ES@OMV, and siAtox1/ES@OMV with 10 μmol/L $CuCl_2$ in the culture media. Data are represented as the mean ± SD ($n = 3$). (E) Immunoblotting detected the FDX1, LIAS protein level in MDA-MB-231 and 4T1 cells treated with siAtox1@OMV, ES@OMV, and siAtox1/ES@OMV with 10 μmol/L $CuCl_2$ in the culture media. Representative data are shown from three independent experiments. (F) Migration assay of 4T1 cells incubated with siAtox1@OMV, ES@OMV, and siAtox1/ES@OMV with 10 μmol/L $CuCl_2$ in the culture media. Scale bar: 100 μm. *P* values were determined by one-way ANOVA with Tukey's multiple comparisons test in (B−D). $^*P < 0.5$; $^{**}P < 0.01$; $^{***}P < 0.001$.

using confocal laser microscopy (CLSM). The results unveiled a progressive rise in red fluorescence intensity over time (Fig. 3A). Notably, the colocalization coefficient (R^2) between the red fluorescence (siAtox1) and the green fluorescence (LysoTraker) was as low as 0.46 at 6 h, indicating that a considerable amount of siAtox1 had successfully escaped from the lysosomes. Furthermore, OMV was labeled with N-hydroxysuccinimide fluorescein isothiocyanate (NHS-FITC) and then electroporated with siAtox1 and ES, resulting in FITC-siAtox1/ES@OMV. The FITC intensity of 4T1 cells at 0, 1, and 6 h post-incubation was semi-quantitatively analyzed using flow cytometry. The results showed that siAtox1/ES@OMV (green fluorescence intensity) at 6 h post-incubation was 4-fold higher than that of the control group (Fig. 3B), indicating the efficient uptake by 4T1 cells. Next, we evaluated the *Atox1* knockdown efficiency using RT-qPCR and found a notable downregulation of *Atox1* mRNA levels after siAtox1@OMV and siAtox1/ES@OMV treatment compared to the PBS or ES@OMV groups (Fig. 3C).

We next sought to assess the cytotoxicity of siAtox1/ES@OMV using a CCK8 assay. Our results showed that siAtox1/

ES@OMV induced a markedly higher level of cell death in comparison to the other treatment groups in conditioned cell culture (10 μmol/L $CuCl_2$ supplemented condition) (Fig. 3D). A high level of copper destabilizes iron-sulfur (Fe−S) cluster proteins within the tricarboxylic acid cycle (TCA), resulting in proteotoxic stress and ultimately cuproptosis[32]. Our results show that, indeed, the levels of Fe−S cluster proteins (hallmarks of cuproptosis[32]), such as lipoic acid synthetase (LIAS) and ferredoxin 1 (FDX1), were decreased in both 4T1 and MDA-MB-231 after siAtox1/ES@OMV treatment (Fig. 3E), indicating that siAtox1/ES@OMV induced efficient cuproptosis in breast cancer cells. Consistently, 4T1 cell migration was also significantly inhibited after the treatment of siAtox1/ES@OMV (Fig. 3F).

To further elucidate the mechanism underlying siAtox1/ES@OMV-induced cuproptosis, we investigated the immunogenicity following OMV treatment in bone marrow-derived DCs (BMDCs). BMDCs express diverse pattern recognition receptors that facilitate the recognition of pathogen-associated molecular patterns (PAMPs) present on the surface of OMV. To evaluate the immunogenicity of siAtox1/ES@OMV, bone marrow-derived DCs (BMDCs) were treated with siAtox1@OMV, ES@OMV, or siAtox1/ES@OMV, respectively. We measured the expression of activation and maturation markers (CD80, CD86, MHC-I, and MHC-II) on BMDCs and analyzed the production of inflammatory cytokines (IL-6, TNF-α, and IFN-β) in the supernatant using ELISA (Fig. 4A). While all OMV-containing formulations significantly increased the secretion of IL-6 (Fig. 4B), TNF-α (Fig. 4C), and IL-1β (Fig. 4D), as well as the expression of CD80, CD86, MHC-I, and MHC-II (Fig. 4E and F), siAtox1/ES@OMV exhibited the strongest immunostimulatory potency compared to siAtox1@OMV or ES@OMV alone. These findings collectively highlight the potent immunostimulatory potential of siAtox1/ES@OMV. Additionally, we observed elevated ROS levels in cells treated with siAtox1/ES@OMV (Fig. 4G), suggesting that ROS generation plays a critical role in mediating copper-induced cell death. These findings provide further mechanistic insights into how siAtox1/ES@OMV induces cuproptosis through the reduction of Fe−S cluster proteins, immune activation, and ROS-mediated pathways.

3.4. In vivo distribution and anti-tumor effects of siAtox1/ES@OMV

To evaluate the *in vivo* tumor-targeting ability of siAtox1/ES@OMV, we intravenously administered ^{Cy5}siAtox1/ES@OMV or free ^{Cy5}siAtox1 (with equivalent siRNA content) into 4T1 tumor-bearing mice. Following a 24-h period, we found significant fluorescent signals within tumor tissues in mice administered with ^{Cy5}siAtox1/ES@OMV compared to free ^{Cy5}siAtox1 (Fig. 5A), suggesting the efficient trafficking of ^{Cy5}siAtox1 into tumor tissues facilitated by OMV-enabled delivery. Subsequent *ex vivo* imaging consistently showed that the fluorescence intensity in tumors from ^{Cy5}siAtox1/ES@OMV-treated mice was 2-fold higher than that from the free ^{Cy5}siAtox1 group (Fig. 5B). Additionally, ^{Cy5}siAtox1/ES@OMV was predominantly localized in tumor tissues compared to major organs, except for the liver (Fig. 5B). Given the remarkable targeting ability to tumor tissues, we next analyzed the *in vivo* knockdown efficiency in tumors using RT-qPCR and showed significant downregulation of *Atox1* mRNA levels in both the siAtox1@OMV and siAtox1/ES@OMV groups (Fig. 5C). By contrast, no significant changes were observed in other tissues, including heart, liver, spleen, lung, and kidney (Supporting Information Fig. S4). These findings underscore the efficient delivery of siAtox1 to the tumor through the systemic route.

We next determined the antitumor efficacy of siAtox1/ES@OMV in a 4T1 breast cancer mouse model. BALB/c mice were subcutaneously inoculated with 4T1 cells in their flank on Day 0, followed by tail vein injections of PBS, siAtox1@OMV, ES@OMV, and siAtox1/ES@OMV on Days 4, 7, 10, 14, and 18, for a total of five administrations (Fig. 5D). We have conducted an additional experiment to determine the optimal treatment dose. Our results showed that a low dose of 20 μg siAtox1/ES@OMV per mouse did not exhibit therapeutic efficacy, while a high dose of 100 μg per mouse led to slight mouse piloerection, and reduced food intake, indicating potential toxicity (Supporting Information Fig. S5). Based on these observations, we selected a dose of 60 μg per mouse, which demonstrated both safety and efficacy in our model. By daily observation of tumor volumes during the treatment period, we found that administration of siAtox1/ES@OMV exhibited superior antitumor efficacy in comparison to both the control and monotherapy group (*i.e.*, siAtox1@OMV or ES@OMV group) (Fig. 5E and F). The synergistic index of siAtox1/ES@OMV is 0.8, indicating a synergistic effect of the combination treatment. Specifically, the average tumor weight of mice treated with siAtox1/ES@OMV was approximately 50% of that in PBS-treated mice (Fig. 5G), while no significant variations in body weight were observed among all treatment groups (Fig. 5H).

We also included free ES to compare the specificity and efficacy with siAtox1/ES@OMV. siAtox1/ES@OMV demonstrated a significantly stronger inhibitory effect on tumor growth compared to free ES when applied at an equivalent ES dose (Supporting Information Fig. S6).

To evaluate the potential advantages of siAtox1/ES@OMV, we compared its efficacy with cisplatin, a widely used chemotherapeutic agent. Our results showed that siAtox1/ES@OMV achieved comparable tumor inhibition efficacy to cisplatin. However, siAtox1/ES@OMV demonstrated significantly lower systemic toxicity, as evidenced by stable body weight in treated subjects, in contrast to the significant weight loss observed after cisplatin treatment (Supporting Information Fig. S7).

3.5. siAtox1/ES@OMV induced cuproptosis and reprogrammed tumor microenvironment to activate anti-tumor immune responses

The hematoxylin and eosin (H&E) staining and terminal deoxynucleotidyl transferase-mediated dUTP-biotin nick end labeling (TUNEL) staining were conducted to examine morphological changes and cell apoptosis. Consistent with the cytotoxicity *in vitro*, more extensive nuclear fragmentation and nucleolysis in the tumor cells of mice treated with siAtox1/ES@OMV were observed compared to those treated with other drugs (Fig. 6A). Meanwhile, immunohistochemistry images revealed a decrease in LIAS levels in the siAtox1/ES@OMV group compared to other treatment groups, indicating siAtox1/ES@OMV successfully induced cuproptosis in the tumor (Fig. 6B). A notable TUNEL-positive signal was found from the siAtox1/ES@OMV-treated tumors (Fig. 6C). Nevertheless, there were no notable alterations in serum biomarkers, such as serum creatine (CK) and alanine transaminase (ALT), or histopathological characteristics of major organs (Supporting Information Fig. S8). Taken together, these results demonstrated siAtox1/ES@OMV significantly inhibited tumor growth through specific induction of cuproptosis and apoptosis in the tumor, without introducing obvious systemic

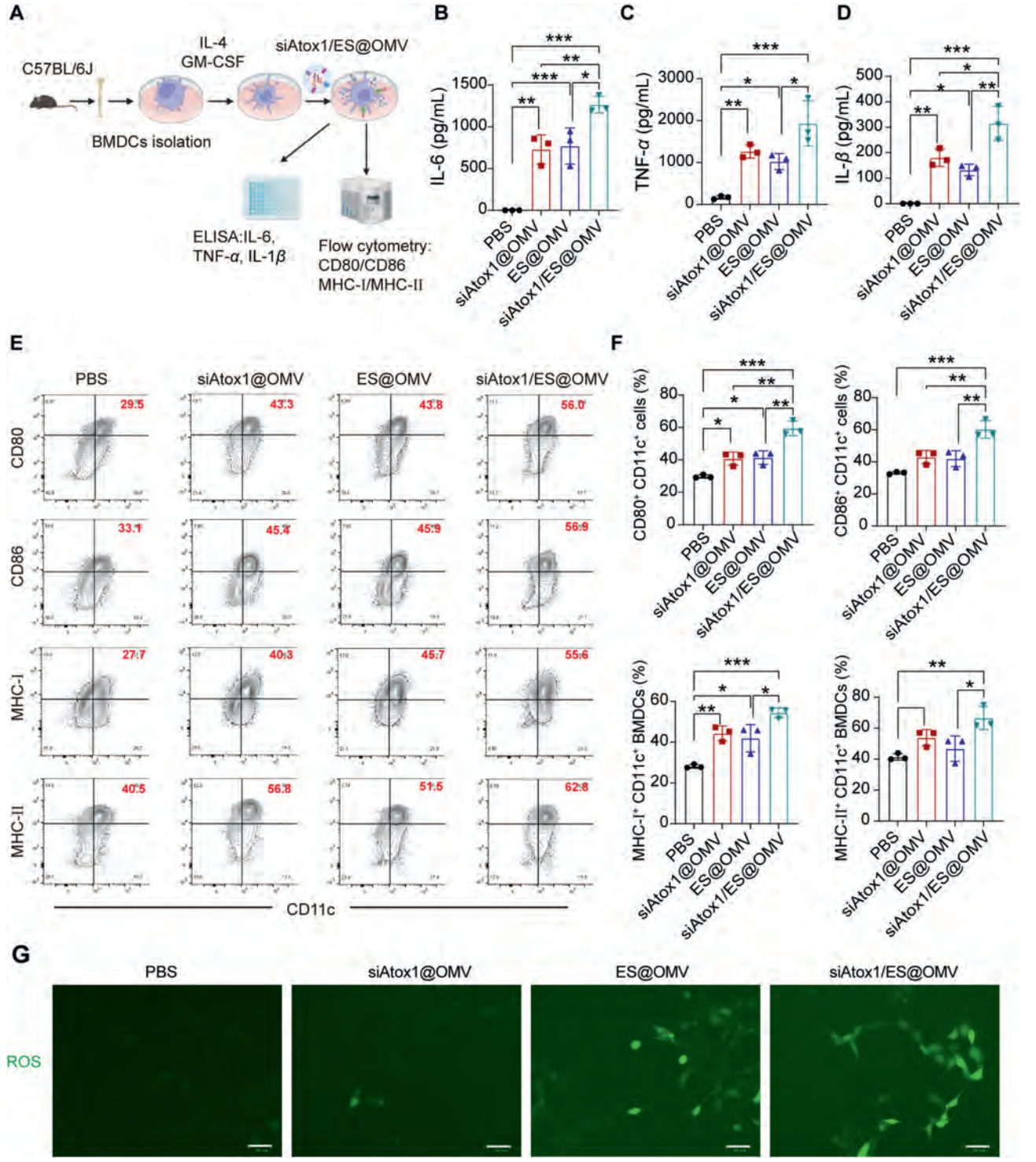

Figure 4 Immunostimulatory effects of siAtox1/ES@OMV. (A) Schematic workflow of the experiment. BMDCs were isolated and treated with siAtox1@OMV, ES@OMV, or siAtox1/ES@OMV (20 μg/mL). After 12 h of treatment, the supernatants were collected for cytokine analysis. After 24 h of treatment, the cells were harvested for flow cytometry analysis. (B−D) Levels of pro-inflammatory cytokines (IL-6, TNF-α, and IFN-β) in the supernatants of BMDCs with indicated treatment for 12 h. Data are represented as the mean ± SD ($n = 3$). (E, F) Representative flow cytometry contour plot (E) and the quantification of the percentages of $CD80^+$, $CD86^+$, MHC-I^+, and MHC-II^+ BMDCs (F) after treatment with 20 μg/mL siAtox1@OMV, ES@OMV, and siAtox1/ES@OMV for 24 h. Data are represented as the mean ± SD ($n = 3$). (G) Representative CLSM images of ROS generation in cells with indicated treatments. Scale bar: 50 μm. Data are represented as the mean ± SD ($n = 3$). *P* values were determined by one-way ANOVA with Tukey's multiple comparisons test in (B−D, F). $^*P < 0.5$; $^{**}P < 0.01$; $^{***}P < 0.001$.

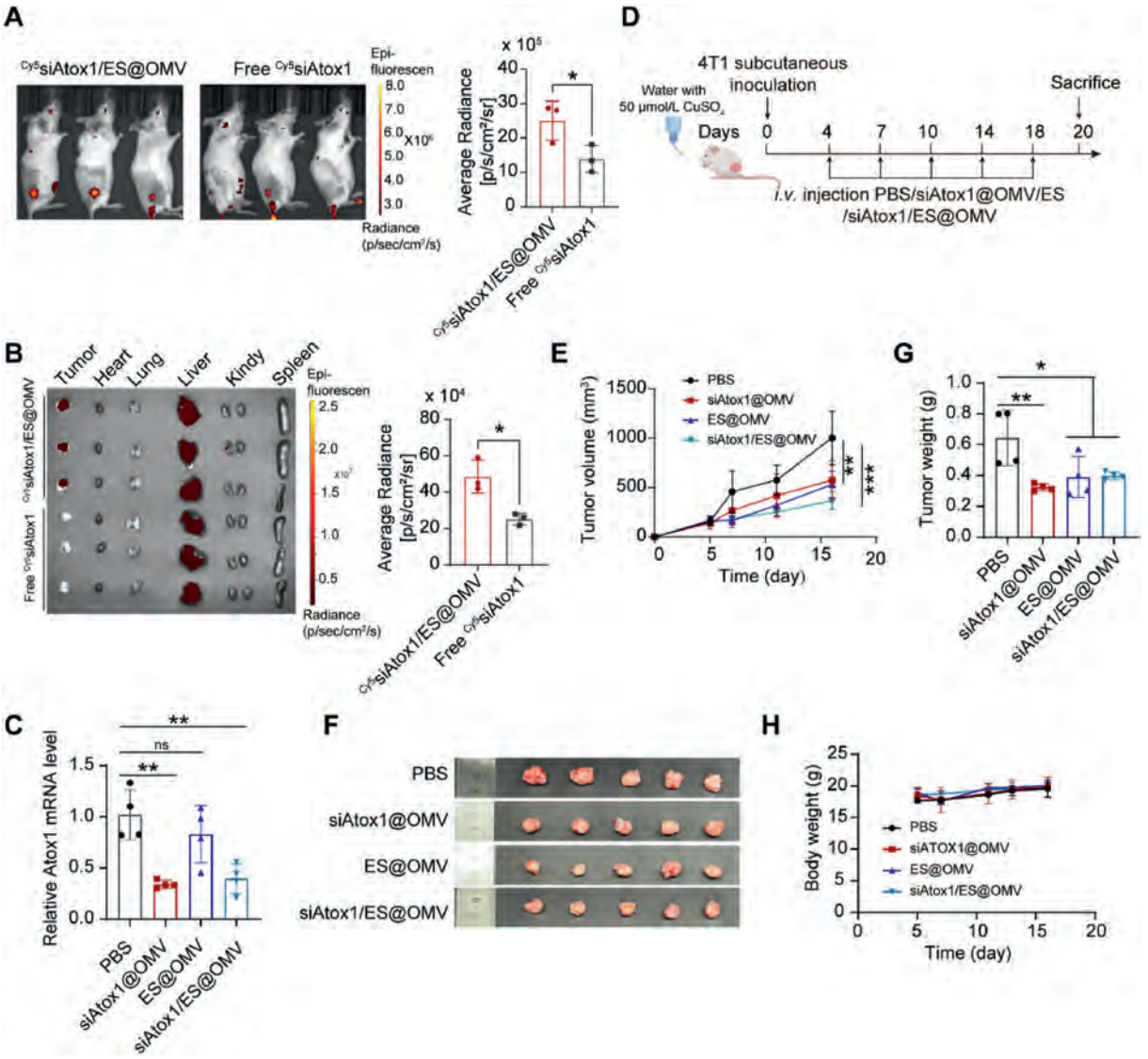

Figure 5 *In vivo* biodistribution and anti-tumor effects of siAtox1/ES@OMV. (A) *In vivo* fluorescent images of 4T1 tumor-bearing mice at 24 h post i.v. injection of Cy5-labled siAtox1@OMV or free siAtox1. Quantification of the fluorescence intensity of Cy5 was shown in the right panel. Data are represented as the mean ± SD ($n = 3$). (B) Biodistribution of Cy5-labeled siAtox1@OMV in tumor, heart, lung, liver, kidney, and spleen at 24 h post i.v. injection. Quantitative analysis of Cy5 fluorescence intensity in tumors was shown in the right panel. Data are represented as the mean ± SD ($n = 3$). (C) RT-qPCR analysis of the relative *Atox1* mRNA expression in tumor tissues from the indicated groups. Data are represented as the mean ± SD ($n = 4$). (D) Schematic for the 4T1 subcutaneous animal model experiment. Female BALB/c mice were subcutaneously (s.c.) injected with 4T1 cells (2×10^6 per mouse) on Day 0, followed by tail vein injection of PBS, siAtox1@OMV, ES@OMV, and siAtox1/ES@OMV on Days 4, 7, 10, 14, and 18 (total of five times). (E) Tumor growth curve of subcutaneously implanted 4T1 tumors bearing mice given the indicated treatment ($n = 5$ mice per group). (F) Pictures of the tumors at the endpoint (Day 20) of the experiment. (G) Average tumor weights at the endpoint (Day 20) of the experiment. (H) Average body weight of BALB/c mice with the indicated treatments. Data are represented as the mean ± SD ($n = 4$). *P* values were determined by one-way ANOVA with Tukey's multiple comparisons test in (A, B, C, F, and G). $^*P < 0.5$; $^{**}P < 0.01$; $^{***}P < 0.001$.

toxicity associated with siAtox1/ES@OMV treatment. By contrast, when introducing excess copper in a non-targeted fashion, such as feeding the mice with a high-copper diet (50 μmol/L $CuSO_4$ in drinking water), we showed that the tumors developed even faster than the regular-diet feeding ones, indicating the necessity of targeted induction of cuproptosis for tumor therapy (Supporting Information Fig. S9).

The significant induction of both cuproptosis and apoptosis and the inherent immunomodulation ability of OMV were assumed to activate anti-tumor immune responses. Therefore, we next explore the systemic and local immune responses after siAtox1/ES@OMV treatment. First, mouse serum was collected for cytokine measurements at 3 h post the last administration. We found an increase in serum IL-6 and IFN-α levels after siAtox1@OMV, ES@OMV, and siAtox1/ES@OMV treatments (Fig. 6D and E). The immune profiling using flow cytometry showed notable infiltrations of immune cells, including $CD45^+CD3^+$T cells, $CD8^+$T cells, and effector $CD8^+$ T ($CD45^+CD3^+CD8^+$IFN-γ^+) populations in

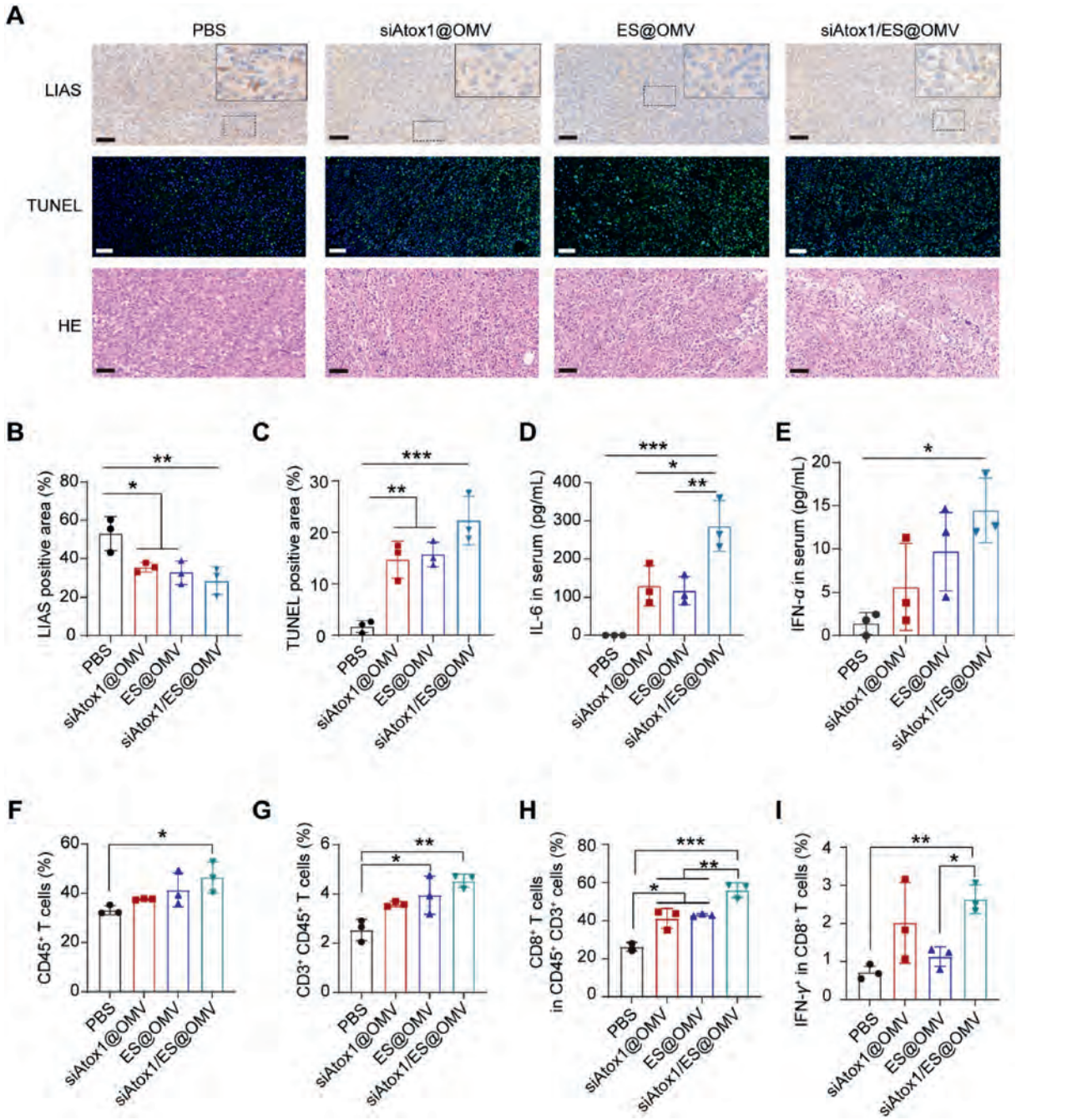

Figure 6 siAtox1/ES@OMV induced cuproptosis and immune cells infiltration in 4T1 tumors *in vivo*. (A) Representative of immunohistochemical staining of the LIAS and TUNEL staining of tumor tissues from the different treatment groups. Scale bar: 50 μm. (B, C) Quantification of LIAS (B) and TUNEL (C) positive areas. Data are represented as the mean ± SD ($n = 3$). (D, E) Serum levels of IL-6 (D) and IFN-α (E) in BALB/c mice at 3 h after systemic administration of PBS, siAtox1@OMV, ES@OMV, or siAtox1/ES@OMV. Data are represented as the mean ± SD ($n = 3$). (F–I) Flow cytometry analysis of immune cell ratios in tumor tissue: $CD45^+$ cells (F), $CD3^+$ $CD45^+$ T cells (G), $CD8^+$ T cells (gated on $CD45^+CD3^+$ cells) (H), and IFN-γ^+ in $CD8^+$ T cells (I). Data are represented as the mean ± SD ($n = 3$). *P* values were determined by one-way ANOVA with Tukey's multiple comparisons test in (B–I). $^*P < 0.5$; $^{**}P < 0.01$; $^{***}P < 0.001$.

tumors treated with siAtox1/ES@OMV compared to the PBS group (Fig. 6F and G, and Supporting Information Fig. S10). Compared to monotherapy (ES@OMV), siAtox1/ES@OMV induced significant $CD8^+$ T cells (1.3-fold), and cytotoxic T cells (2.3-fold) (Fig. 6H and I). Taken together, siAtox1/ES@OMV has effectively reprogrammed the TME, leading to the activation of a systemic anti-tumor immune response.

3.6. siAtox1/ES@OMV inhibits tumor growth in an orthotopic CT26 colon tumor model

To test the therapeutic potential of siAtox1/ES@OMV across other tumor types, an orthotopic CT26-Luc colon tumor model was established in BALB/c mice as performed by Rapic et al.[33] PBS or siAtox1/ES@OMV was administered *via* tail vein injection on

Days 7, 10, 13, 16, and 18 after the orthotopic implantation of the CT26-Luc tumor (Fig. 7A). Tumor growth was monitored 2−3 times per week using IVIS imaging. The siAtox1/ES@OMV group exhibited a significantly delayed tumor growth rate compared to the PBS group, as evidenced by bioluminescence imaging (BLI) measurements (Fig. 7B and Supporting Information Fig. S11A). Consistently, the tumor volume and weight in the siAtox1/ES@OMV group were significantly lower than those in the PBS group at the endpoint (Fig. 7C and D). The treatment was well-tolerated, with no significant weight loss observed in the treated mice (Fig. S11B). Furthermore, the overall intestinal morphology of mice in both groups remained unchanged, with the intestinal structure intact and no evidence of significant damage or abnormalities (Fig. S11C). These findings suggest that siAtox1/ES@OMV treatment is effective and biocompatible for intestinal tissues. The immune profiling of the tumor immune microenvironment was analyzed by flow cytometry and CyTOF. Flow cytometry revealed that siAtox1/ES@OMV treatment increased the total macrophage population and decreased the M2 macrophage ratio (Supporting Information Fig. S12A and S12B), indicating siAtox1/ES@OMV promotes macrophage polarization toward the M1 phenotype. To further characterize the immune landscape, we conducted high-dimensional CyTOF analysis using a group of immune cell markers, including CD45, CD11b, CD3,

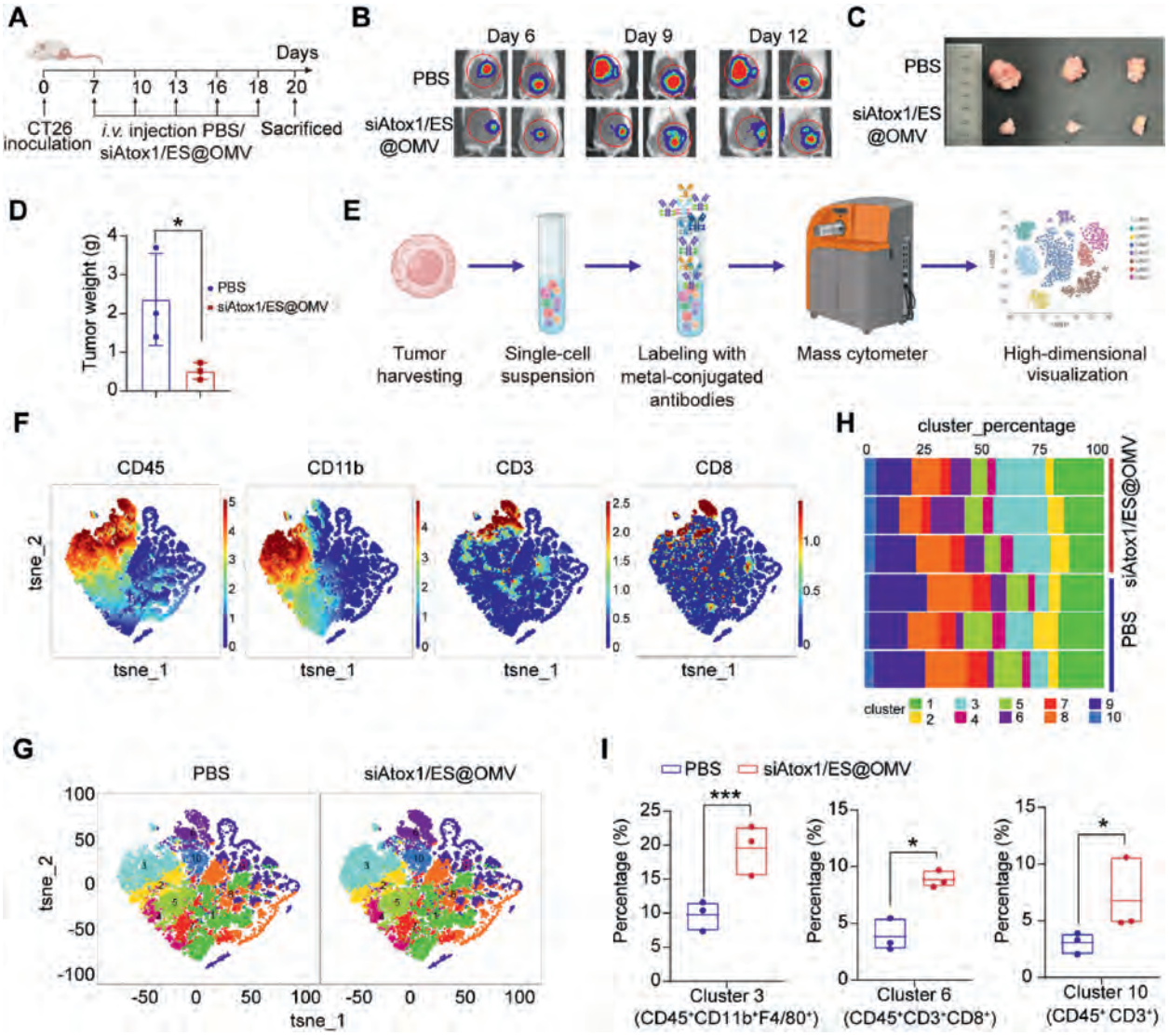

Figure 7 siAtox1/ES@OMV inhibited tumor growth in a CT-26 mouse tumor model. (A) Scheme showing the design of the animal experiments. Female BALB/c mice were orthotopic implanted with CT26-Luc tumor fragments on Day 0, followed by tail vein injection of PBS or siAtox1/ES@OMV on Days 7, 10, 13, 16, and 18 (total of five times). (B) *In vivo* bioluminescence images of mice bearing CT26-Luc tumors at different days. (C, D) Tumor picture (C) and weight (D) at the endpoint of the experiment. Data are represented as the mean ± SD ($n = 3$). (E) Workflow of the CyTOF experiment. (F) *t*-SNE plot of expression levels of selected immune cell surface markers. Colar bar based on the relative intensity of marker expression. (G) *t*-SNE plots of the 10 clusters based on the cell surface marker expression in the PBS or siAtox1/ES@OMV group. (H) The percentage of the 10 clusters in the PBS or siAtox1/ES@OMV group. (I) Boxplots depicting the percentage of key clusters from the indicated groups. Representative data are shown as the mean ± SD ($n = 3$). *P* values were obtained using unpaired two-tailed *t*-tests in D and I. $^{*}P < 0.05$; $^{**}P < 0.01$.

CD4, and CD8 (Fig. 7E). The distribution of immunological markers (CD45, CD11b, CD3, and CD8) was visualized through *t*-SNE plots (Fig. 7F). We identified a total of 10 clusters in tumors using *t*-SNE analyses (Fig. 7G, Fig. S12C). The percentage of each cluster was depicted in Fig. 7H. Compared to the PBS group, the percentage of Clusters 3 ($CD45^+CD11b^+F4/80^+$), Cluster 6 ($CD45^+CD3^+CD8^+$), and Cluster 10 ($CD45^+CD3^+$) in the siAtox1/ES@OMV group was significantly increased by 2.0-, 2.3-, and 2.2-fold (Fig. 7I), respectively, indicating an elevation of macrophages and $CD8^+$ T cells within the tumor microenvironments following siAtox1/ES@OMV treatment. Taken together, these results demonstrated that siAtox1/ES@OMV effectively inhibited colon tumor growth, promoted immune cell infiltration, and inflamed the tumor immune microenvironment.

4. Discussion

Cuproptosis, a newly discovered form of regulated cell death that relies on copper, presents promising avenues for cancer therapy. However, copper acts as a double-edged sword: it is essential for various biological processes, yet it can also pose significant risks when not properly regulated[34]. Non-specific copper delivery methods are often insufficient for triggering tumor-specific cuproptosis, as they lack the precision needed to control copper levels exclusively within cancer cells[35]. In addition, such non-targeted delivery may unintentionally stimulate tumor growth by supplying copper that enhances cancer cell metabolism and proliferation. This limitation has contributed to the limited success of copper-based therapies in clinical trials, particularly during efficacy validation stages[36]. Our results have shown a high-copper diet significantly promoted tumor growth, suggesting that systemic copper administration promotes cuprogenesis for tumor progression rather than inducing cuproptosis. Therefore, targeted intervention of tumor copper metabolism is recommended for effective cancer treatment[37]. Developing targeted delivery systems that direct copper or modulate copper pathways specifically within tumor cells is crucial for realizing the therapeutic potential of cuproptosis in cancer treatment.

ES-induced cuproptosis is dependent on FDX1 but not FDX2[32,38], which explains why the therapeutic efficacy of copper-dependent cell death varies across different tumor types. We analyzed the expression levels of FDX1 and FDX2 in different cancer types using publicly available databases, including GEPIA and DepMap. The results indicate that the expression of FDX1 is significantly higher than that of FDX2 in BRCA (Breast Invasive Carcinoma) and COAD (Colon Adenocarcinoma) (Supporting Information Fig. S13A). Furthermore, in the breast and colorectal cancer cell lines, we observed that FDX1 expression levels are consistently higher than those of FDX2 (Fig. S13B). This suggests that elesclomol preferentially binds to FDX1 in these cancer types, thereby promoting cuproptosis.

Here, we utilized OMV derived from *Akk* for the co-delivery of ES and *Atox1* siRNA to disrupt copper exportation in tumor cells to improve the efficacy of ES. Previous studies have explored a range of nanocarriers, including micellar nanoparticles, pluronic F127-based cubosomes, and reactive oxygen species (ROS)-sensitive polymers (PHPM), for the delivery of ES and Cu complex[39-42]. While these approaches successfully triggered cuproptosis to a certain extent, the therapeutic effect needs further improvement. In a patient-derived xenograft model of hepatocellular carcinoma, the combination of ES−$CuCl_2$ with small interfering RNA-mediated knockdown of PD-L1 inhibited tumor growth more effectively than ES−$CuCl_2$ alone[42]. This suggests that induction of cuproptosis has the potential to synergy with immunotherapy. Our strategy, by employing immune-stimulatory *Akk*-OMV for the co-delivery of ES and siAtox1, exhibits highly efficient antitumor effects in two representative refractory tumor models (TNBC and orthotopic CT26 colon models). Our delivery system integrates *Akk*-OMV-mediated immune modulation with cuproptosis-inducing therapeutics, offering a dual mechanism for enhanced anti-tumor efficacy.

5. Conclusions

In our study, we harnessed the elevated copper levels in tumors to induce cuproptosis through the targeted dual delivery of siAtox1 and ES. By employing *Akk*-derived OMV as the delivery platform, we not only enhanced copper accumulation but also stimulated the tumor immune microenvironment, promoting T cell infiltration and specific tumor killing. Our strategy offers a promising combinatorial approach for treating high-copper consumption and immune cold tumors.

Acknowledgments

This study was supported by grants from the National Key R&D program of China (2021YFA1201100, 2022YFA1206100, 2022YFA1207300), Beijing Natural Science Foundation (Z230008, L232125, 7242132, China), the National Natural Science Foundation of China (No. 32201158, No. 32271449, No. 82170087).

Author contributions

Muhammad Hamza and Shuai Wang: Investigation, methodology, visualization, writing-original draft. Hao Wu, Jiayi Sun, Yang Du, Chuting Zeng, and Yike Liu: Methodology, visualization and formal analysis. Kun Li and Xili Zhu: Methodology, resources, and validation. Huiying Liu, Lin Chen, and Motao Zhu: Conceptualization, resources, supervision, funding acquisition, visualization, writing-review and editing. All of the authors have read and approved the final manuscript.

Conflicts of interest

The authors have no conflicts of interest to declare.

Appendix A. Supporting information

Supporting information to this article can be found online at https://doi.org/10.1016/j.apsb.2025.03.014.

References

1. Solier S, Muller S, Caneque T, Versini A, Mansart A, Sindikubwabo F, et al. A druggable copper-signalling pathway that drives inflammation. *Nature* 2023;**617**:386−94.
2. Lowndes SA, Harris AL. The role of copper in tumour angiogenesis. *J Mammary Gland Biol Neoplasia* 2005;**10**:299−310.
3. Tsang T, Posimo JM, Gudiel AA, Cicchini M, Feldser DM, Brady DC. Copper is an essential regulator of the autophagic kinases ULK1/2 to drive lung adenocarcinoma. *Nat Cell Biol* 2020;**22**:412−24.

4. Tang D, Kroemer G, Kang R. Targeting cuproplasia and cuproptosis in cancer. *Nat Rev Clin Oncol* 2024;**21**:370−88.
5. Abdelmaksoud NM, Abulsoud AI, Abdelghany TM, Elshaer SS, Rizk SM, Senousy MA. Mitochondrial remodeling in colorectal cancer initiation, progression, metastasis, and therapy: a review. *Pathol Res Pract* 2023;**246**:154509.
6. Oliveri V. Biomedical applications of copper ionophores. *Coordi Chem Rev* 2020;**422**:213474.
7. O'Day SJ, Eggermont AM, Chiarion-Sileni V, Kefford R, Grob JJ, Mortier L, et al. Final results of phase III SYMMETRY study: randomized, double-blind trial of elesclomol plus paclitaxel *versus* paclitaxel alone as treatment for chemotherapy-naive patients with advanced melanoma. *J Clin Oncol* 2013;**31**:1211−8.
8. Zheng P, Zhou C, Lu L, Liu B, Ding Y. Elesclomol: a copper ionophore targeting mitochondrial metabolism for cancer therapy. *J Exp Clin Cancer Res* 2022;**41**:271.
9. Hedley D, Shamas-Din A, Chow S, Sanfelice D, Schuh AC, Brandwein JM, et al. A phase I study of elesclomol sodium in patients with acute myeloid leukemia. *Leuk Lymphoma* 2016;**57**:2437−40.
10. O'Day S, Gonzalez R, Lawson D, Weber R, Hutchins L, Anderson C, et al. Phase II, randomized, controlled, double-blinded trial of weekly elesclomol plus paclitaxel *versus* paclitaxel alone for stage IV metastatic melanoma. *J Clin Oncol* 2009;**27**:5452−8.
11. Monk BJ, Kauderer JT, Moxley KM, Bonebrake AJ, Dewdney SB, Secord AA, et al. A phase II evaluation of elesclomol sodium and weekly paclitaxel in the treatment of recurrent or persistent platinum-resistant ovarian, fallopian tube or primary peritoneal cancer: an NRG oncology/gynecologic oncology group study. *Gynecol Oncol* 2018; **151**:422−7.
12. Prohaska JR. Role of copper transporters in copper homeostasis. *Am J Clin Nutr* 2008;**88**:826-9S.
13. Yang D, Xiao P, Qiu B, Yu HF, Teng CB. Copper chaperone antioxidant 1: multiple roles and a potential therapeutic target. *J Mol Med* 2023;**101**:527−42.
14. La Fontaine S, Mercer JFB. Trafficking of the copper-ATPases, ATP7A and ATP7B: role in copper homeostasis. *Arch Biochem Biophys* 2007;**463**:149−67.
15. Hamza I, Faisst A, Prohaska J, Chen J, Gruss P, Gitlin JD. The metallochaperone Atox1 plays a critical role in perinatal copper homeostasis. *Proc Natl Acad Sci U S A* 2001;**98**:6848−52.
16. Hamza I, Prohaska J, Gitlin JD. Essential role for Atox1 in the copper-mediated intracellular trafficking of the Menkes ATPase. *Proc Natl Acad Sci U S A* 2003;**100**:1215−20.
17. Wang J, Luo C, Shan C, You Q, Lu J, Elf S, et al. Inhibition of human copper trafficking by a small molecule significantly attenuates cancer cell proliferation. *Nat Chem* 2015;**7**:968−79.
18. Krysko DV, Garg AD, Kaczmarek A, Krysko O, Agostinis P, Vandenabeele P. Immunogenic cell death and DAMPs in cancer therapy. *Nat Rev Cancer* 2012;**12**:860−75.
19. Bray F, Laversanne M, Sung H, Ferlay J, Siegel RL, Soerjomataram I, et al. Global cancer statistics 2022: GLOBOCAN estimates of incidence and mortality worldwide for 36 cancers in 185 countries. *CA Cancer J Clin* 2024;**74**:229−63.
20. Squitti R, Pal A, Dhar A, Shamim MA, Ventriglia M, Simonelli I, et al. Serum copper status of patients with colorectal cancer: a systematic review and meta-analysis. *J Trace Elem Med Biol* 2024;**82**:127370.
21. Jouybari L, Kiani F, Islami F, Sanagoo A, Sayehmiri F, Hosnedlova B, et al. Copper concentrations in breast cancer: a systematic review and meta-analysis. *Curr Med Chem* 2020;**27**:6373−83.
22. Xiao Y, Ma D, Zhao S, Suo C, Shi J, Xue MZ, et al. Multi-omics profiling reveals distinct microenvironment characterization and suggests immune escape mechanisms of triple-negative breast cancer. *Clin Cancer Res* 2019;**25**:5002−14.
23. Hashimoto M, Kojima Y, Sakamoto T, Ozato Y, Nakano Y, Abe T, et al. Spatial and single-cell colocalisation analysis reveals MDK-mediated immunosuppressive environment with regulatory T cells in colorectal carcinogenesis. *EBioMedicine* 2024;**103**:105102.
24. Furuyama N, Sircili MP. Outer Membrane Vesicles (OMVs) produced by gram-negative bacteria: structure, functions, biogenesis, and vaccine application. *BioMed Res Int* 2021;**2021**:1490732.
25. Amalia L, Tsai SL. Functionalization of OMVs for biocatalytic applications. *Membranes* 2023;**13**:459.
26. Geerlings SY, Kostopoulos I, de Vos WM, Belzer C. *Akkermansia muciniphila* in the human gastrointestinal tract: when, where, and how?. *Microorganisms* 2018;**6**:75.
27. Yoon HS, Cho CH, Yun MS, Jang SJ, You HJ, Kim Jh, et al. *Akkermansia muciniphila* secretes a glucagon-like peptide-1-inducing protein that improves glucose homeostasis and ameliorates metabolic disease in mice. *Nat Microbiol* 2021;**6**:563−73.
28. Luo ZW, Xia K, Liu YW, Liu JH, Rao SS, Hu XK, et al. Extracellular vesicles from *Akkermansia muciniphila* elicit antitumor immunity against prostate cancer *via* modulation of $CD8^+$ T Cells and macrophages. *Int J Nanomedicine* 2021;**16**:2949−63.
29. Wang X, Lin S, Wang L, Cao Z, Zhang M, Zhang Y, et al. Versatility of bacterial outer membrane vesicles in regulating intestinal homeostasis. *Sci Adv* 2023;**9**:eade5079.
30. Chelakkot C, Choi Y, Kim DK, Park HT, Ghim J, Kwon Y, et al. *Akkermansia muciniphila*-derived extracellular vesicles influence gut permeability through the regulation of tight junctions. *Exp Mol Med* 2018;**50**:e450.
31. Ansaldo E, Slayden LC, Ching KL, Koch MA, Wolf NK, Plichta DR, et al. *Akkermansia muciniphila* induces intestinal adaptive immune responses during homeostasis. *Science* 2019;**364**:1179−84.
32. Tsvetkov P, Coy S, Petrova B, Dreishpoon M, Verma A, Abdusamad M, et al. Copper induces cell death by targeting lipoylated TCA cycle proteins. *Science* 2022;**375**:1254−61.
33. Rapic S, Vangestel C, Verhaeghe J, Van den Wyngaert T, Hinz R, Verhoye M, et al. Characterization of an orthotopic colorectal cancer mouse model and its feasibility for accurate quantification in positron emission tomography. *Mol Imaging Biol* 2017;**19**:762−71.
34. Vetchý M. Biological role of copper as an essential trace element in the human organism. *Ceska Slov Farm* 2018;**67**:143−53.
35. Abdullah KM, Kaushal JB, Takkar S, Sharma G, Alsafwani ZW, Pothuraju R, et al. Copper metabolism and cuproptosis in human malignancies: unraveling the complex interplay for therapeutic insights. *Heliyon* 2024;**10**:e27496.
36. Aishajiang R, Liu Z, Wang T, Zhou L, Yu D. Recent advances in cancer therapeutic copper-based nanomaterials for antitumor therapy. *Molecules* 2023;**28**:2303.
37. Yang Y, Li M, Chen G, Liu S, Guo H, Dong X, et al. Dissecting copper biology and cancer treatment: 'activating cuproptosis or suppressing cuproplasia'. *Coord Chem Rev* 2023;**495**:215395.
38. Kirshner JR, He S, Balasubramanyam V, Kepros J, Yang CY, Zhang M, et al. Elesclomol induces cancer cell apoptosis through oxidative stress. *Mol Cancer Ther* 2008;**7**:2319−27.
39. Wang Q, Huang CH, Wibowo FS, Amin R, Shen J, Li F, et al. Elesclomol-copper nanoparticles overcome multidrug resistance in cancer cells. *ACS Appl Mater Inter* 2024;**16**:13509−24.
40. Faria AR, Silvestre OF, Maibohm C, Adão RMR, Silva BFB, Nieder JB. Cubosome nanoparticles for enhanced delivery of mitochondria anticancer drug elesclomol and therapeutic monitoring *via* sub-cellular NAD(P)H multi-photon fluorescence lifetime imaging. *Nano Res* 2019;**12**:991−8.
41. Guo B, Yang F, Zhang L, Zhao Q, Wang W, Yin L, et al. Cuproptosis induced by ROS responsive nanoparticles with elesclomol and copper combined with αPD-L1 for enhanced cancer immunotherapy. *Adv Mat* 2023;**35**:e2212267.
42. Shen W, Pei P, Zhang C, Li J, Han X, Liu T, et al. A polymeric hydrogel to eliminate programmed death-ligand 1 for enhanced tumor radio-immunotherapy. *ACS Nano* 2023;**17**:23998−4011.